A Highly Reactive $Co^{III,IV}_2(\mu\text{-}O)_2$ Diamond Core Complex that Cleaves C-H Bonds

Yan Li[1], Suhashini Handunneththige[2], Erik R. Farquhar[3,4], Yisong Guo[5], Marat R. Talipov[2]*, Feifei Li[2]* and Dong Wang[1]*

[1] Department of Chemistry and Biochemistry, Center for Biomolecular Structure and Dynamics, University of Montana, Missoula, MT 59803, USA

[2] Department of Chemistry and Biochemistry, New Mexico State University, Las Cruces, NM 88003, USA

[3] CWRU Center for Synchrotron Biosciences, NSLS-II, Brookhaven National Laboratory, Upton, NY 11973, USA

[4] School of Medicine, Case Western Reserve University, Cleveland, OH 44106, USA

[5] Department of Chemistry, Carnegie Mellon University, Pittsburgh, PA 15213, USA

ABSTRACT: The selective activation of strong sp^3 C–H bonds at mild conditions is a key step in many biological and synthetic transformations, and an unsolved challenge for synthetic chemists. In nature, soluble methane monooxygenase (sMMO) is one representative example of nonheme dinuclear iron-dependent enzymes that activate strong sp^3 C–H bonds by a high-valent diiron(IV) intermediate **Q**. To date, synthetic model complexes of sMMO-**Q** have shown limited abilities to oxidize strong C–H bonds. In this work, we generated a high-valent $Co^{III,IV}_2(\mu\text{-}O)_2$ complex **3** supported by a tetradentate TPA ligand via one-electron oxidation of its $Co^{III}_2(\mu\text{-}O)_2$ precursor **2**. Characterization of **2** and **3** using X-ray absorption spectroscopy and DFT calculations showed that both species possess a diamond core structure with a short Co•••Co distance of 2.78 Å. Furthermore, **3** is an EPR active species showing an $S = 1/2$ signal with clear hyperfine splittings originated from the coupling of the ^{59}Co nuclear spin with the electronic spin. Importantly, **3** is a highly reactive oxidant for sp^3 C–H bonds, and an oxygenation reagent. **3** has the highest rate constant (1.5 M^{-1} s^{-1} at -60 ºC) for oxidizing 9,10-dihydroanthracene (DHA) compared to diamond core complexes of other first-row transition metals including Mn, Fe and Cu reported previously. Specifically, **3** is about 4-5 orders of magnitude more reactive than the diiron analogs $Fe^{III,IV}_2(\mu\text{-}O)_2$ and $Fe^{IV}_2(\mu\text{-}O)_2$ supported by TPA and related ligands. These findings shed light on future development of more reactive approaches for C–H bond activation by bio-inspired dicobalt complexes.

Introduction.

The activation of carbon-hydrogen (C–H) bonds is the first step of functionalizing inert hydrocarbons. This transformation is a key step in many biological and synthetic processes.[1-7] Nature offers highly efficient and selective solutions for carrying out aliphatic C–H bond functionalization using metalloenzymes that employ earth-abundant transition metals such as iron and copper in the active sites.[8] One representative example is soluble methane monooxygenase (sMMO), a nonheme dinuclear iron-dependent enzyme that catalyzes the hydroxylation of the strong C–H bond of methane (bond dissociation energy BDE = 105 kcal/mol) using O_2 as the oxidant.[9-10] The catalytic cycle of sMMO has been extensively studied over decades, and features a high-valent bis-μ-oxo $Fe^{IV}_2(\mu\text{-}O)_2$ "diamond core" intermediate called **Q** as the active oxidant for C–H bond activation. Spectroscopic characterization of sMMO-**Q** has revealed that the $Fe^{IV}_2(\mu\text{-}O)_2$ diamond core has a short Fe•••Fe distance of 2.46 Å,[11] with both Fe centers in a high spin ($S = 2$) state.[12-13] Lipscomb and co-workers have further provided confirmative evidence using resonance Raman spectroscopy for the structural assignment of sMMO-**Q**.[14] However, recent work by DeBeer et al. employing high-energy-resolution fluorescence detected X-ray absorption spectroscopy (HERFD XAS) argued that sMMO-**Q** possesses an open core structure with an Fe•••Fe distance of ~3.4 Å based on HERFD XAS data.[15-16] On the other hand, synthetic high-valent model complexes of sMMO-**Q** have been reported. A number of dinuclear μ-oxo and bis-μ-oxo manganese,[17-20] iron[9,21-22] and copper[23-24] complexes exhibited C–H bond cleavage and O–O bond formation activities. However, only one of them, a (μ-oxo)diiron(IV) complex supported by an anionic pentadentate N4O ligand, is capable of activating strong sp^3 C–H bonds such as those in cyclohexane (BDE = 99.3 kcal/mol).[21]

In contrast, the high-valent diamond core chemistry of cobalt has been much less investigated, likely due to the difficulty of generating high-valent oxocobalt(IV) species for characterization.[25-26] There is evidence showing that high-valent oxocobalt(IV) species are involved in a number of water oxidation[27-28] and C–H bond cleavage reactions.[29] To date, six $Co^{III}_2(\mu\text{-}O)_2$ complexes supported by tridentate or bidentate ligands have been structurally characterized.[30-35] However, no higher-valent derivative is available. In the present study, we report an unprecedented high-valent $Co^{III,IV}_2(\mu\text{-}O)_2$ complex (**3**) supported by a tetradentate tris(2-pyridylmethyl)amine (TPA) ligand (Scheme 1). This species can be generated by one-electron oxidation of its $Co^{III}_2(\mu\text{-}O)_2$ precursor (**2**). Characterization of **3** using combined spectroscopic and computa-

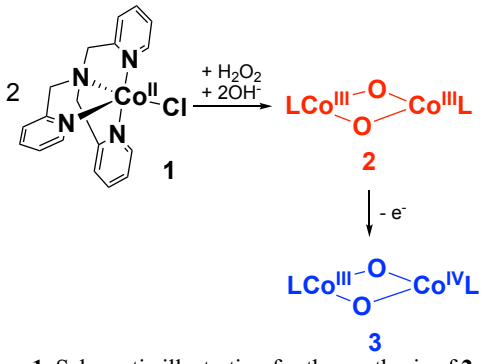

Scheme 1. Schematic illustration for the synthesis of **2** and **3**.

tional approaches confirmed that it has a diamond core structure with a short Co•••Co distance of 2.78 Å. More importantly, **3** is highly reactive and activates C–H bonds at a rate constant that is 3-5 orders of magnitude higher than its diiron and dimanganese analogs measured at higher temperatures.

Results and discussion.

Generation and characterization of 2. Instead of first making the dihydroxo-bridged dicobalt(II) precursor $Co^{II}_2(\mu\text{-}OH)_2$ described by Hikichi *et al.*,[36] we hypothesized that the direct reaction of a mononuclear cobalt(II)-Cl species $[(TPA)Co^{II}\text{-}Cl]^+$ (**1**)[37] with H_2O_2 in the presence of base could afford the diamond core complex $[(TPA)Co^{III}(\mu\text{-}O)_2Co^{III}(TPA)]^{2+}$ (**2**) according to Eq.1.

$$2[(TPA)Co^{II}\text{-}Cl]^+ + H_2O_2 + 2OH^- \rightarrow [(TPA)Co^{III}(\mu\text{-}O)_2Co^{III}(TPA)]^{2+} + 2H_2O + 2Cl^- \quad (1)$$

Indeed, the reaction of **1** directly with 0.5 eq. H_2O_2 at -40 °C in the presence of 1 eq. tetrabutylammonium hydroxide as the base produced a new brown species **2** (Figure 1 red). **2** exhibits an intense absorption at 460 nm (ε = 4700 M^{-1} cm^{-1}) and a weak shoulder at ~600 nm. No reaction was observed between **1** and H_2O_2 alone. The stoichiometry between **1**, H_2O_2, and OH^- was determined to be 2:1:2 by a titration experiment (Figure S1). The addition of excess H_2O_2 or OH^- did not cause **2** to be formed in a higher yield. The formation of **2** could be carried out in a variety of solvents including acetonitrile (MeCN), methanol (MeOH) and dichloromethane (DCM). **2** is relatively stable at -40 °C and below ($t_{1/2}$ = ~4 hours at -40 °C), and undergoes fast thermal decay at higher temperatures. Above -20 °C, **2** is formed at much reduced yields. **2** has a much lower thermal stability compared to the μ-hydroxo, μ-1,2-peroxo-bridged dicobalt(III) species of the same TPA ligand, whose single crystals can be obtained at room temperature.[38-39] The optical features of **2** are distinct from those reported for $Co^{III}_2(\mu\text{-}OH)_2$, $Co^{III}(\mu\text{-}OH)(\mu\text{-}OO)Co^{III}$ and mononuclear cobalt(III)-peroxo species $Co^{III}(O_2)$.[38,40-45] In contrast, the intensity of the 460 nm absorption resembles those of the $Co^{III}_2(\mu\text{-}O)_2$[30-31,35] and $Ni^{III}_2(\mu\text{-}O)_2$[46-47] complexes reported previously, which was assigned to an oxo-to-metal charge transfer transition.

The characterization of **2** using high-resolution electrospray ionization mass spectrometry (ESI-MS) shows a primary signal at *m/z* = 884.1755 (Figure S2). The mass and the isotope distribution pattern correspond to $[Co^{III}_2(TPA)_2(O)_2(CF_3COO)(CH_3CN)]^+$. When the formation of **2** was carried out using ^{18}O labeled H_2O_2, the ESI-MS signal was observed at *m/z* 888.2312. This upshift of four mass units clearly indicates that the oxygen atoms from H_2O_2 are

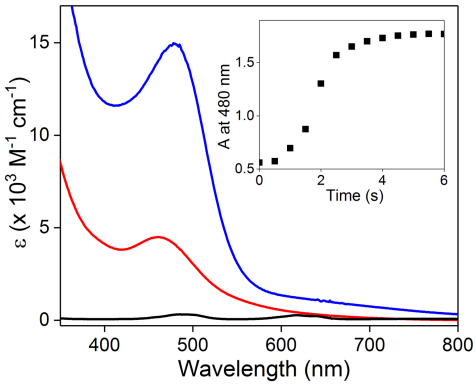

Figure 1. Optical spectra of **1** (black), **2** (red) and **3** (blue) obtained in methanol at -60 °C. Inset: time trace of the absorption at 480 nm during the formation of **3**.

incorporated into the molecular formula of **2**. Complex **2** is EPR silent, consistent with the assignment of two d^6 Co(III) centers (Figure S3). In contrast, the mononuclear precursor **1** exhibited an EPR signal typical of d^7 S = 3/2 Co(II).[48-49] The lack of any residual Co(II) signal in the spectrum of **2** indicates that the conversion of **1** to **2** is complete. Furthermore, characterization of **2** using ^1H NMR spectroscopy at -55 °C in methanol confirmed that **2** is a diamagnetic species (Figure S4). Interestingly, we observed two sets of signals assignable to pyridine aromatic protons with the integration ratio of 2:1. This is clear evidence that the three pyridines of each TPA ligand are in two different environments---likely two are *trans*- to each other and the third one is *trans* to a bridging oxo ligand, a pattern that resembles that of the $Co^{III}_2(\mu\text{-}OH)_2$ species supported by the same TPA ligand.[40] Quantification by integrating the aromatic proton signals using 4,4-dimethyl-4-silapentane-1-sulfonic acid (DSS) as the internal standard showed that the formation of **2** is quantitative (> 90%).

Generation and characterization of 3. To obtain a high-valent derivative of **2**, we employed a one-electron chemical oxidant Ce^{IV} (in the form of $(NH_4)_2Ce(NO_3)_6$, CAN).[50] The introduction of 2- to 3-fold excess of CAN into the methanol solution of **2** at -60 °C and below afforded a new, transient species **3** with an intense absorption maximum at 480 nm (Figure 1 blue). **3** was formed from **2** within seconds (Figure 1, inset), much faster than the formation of **2** from **1** at -40 °C. **3** is less stable than **2** and decomposes even at -60 °C ($t_{1/2}$ = ~90 s at -60 °C), indicating that **3** is likely a higher-valent species. Furthermore, **3** is much less stable than the superoxo-bridged dicobalt(III) species of the TPA ligand, which can be obtained by one-electron oxidation of the peroxo-dicobalt(III) precursor and characterized at room temperature.[38-39] **3** can be reduced back to **2** using ferrocene (Figure S5) and acetylferrocene (E = 0.27 V), but not diacetylferrocene (E = 0.49 V). The one-electron redox potential of **3** was thus estimated to fall in the range of 0.27-0.49 V vs. ferrocene.

3 is an EPR active species, showing a broad X-band (9.65 GHz) EPR signal at g = 2.13, 2.03 and 1.99 measured at 16 K, which is indicative of an S = 1/2 system (Figure 2 blue). The quantification of this S = 1/2 signal revealed that **3** was formed in a typical yield of ~70-80% from **2**. Based on the EPR spin quantification, the molar extinction coefficient of the 480 nm band is estimated to be ~15,000 M^{-1} cm^{-1}. We performed careful control experiments to exclude possible interference from CAN and its one-electron reduced species (both are EPR silent). Due to the broadness of this EPR signal, the hyperfine

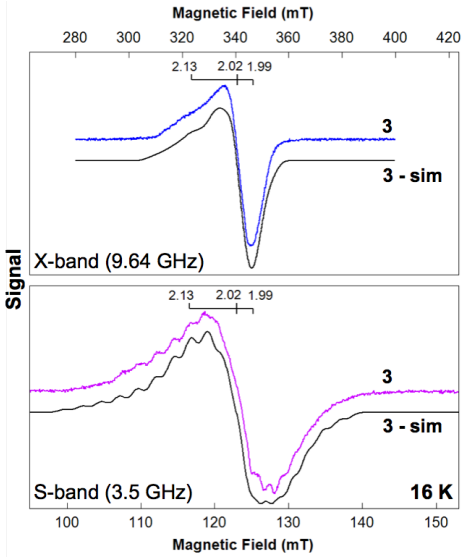

Figure 2. X-band (blue) and S-band (purple) EPR spectra of **3** recorded at 16 K. The spectra are aligned against g = 2 marker. The spectral simulations for the corresponding EPR signal are shown in black underneath the experimental spectra. The simulation parameters for **3** are g = [2.13, 2.02, 1.99], σ_g = [0.01, 0.008, 0.008], A(^{59}Co) = [75, 35, 18] MHz, with Euler angle [α, β, γ] = [0, 20°, 0], line width = 0.7 mT. The measurement conditions: microwave frequency, 9.64 GHz (X-band) and 3.5 GHz (S-band); microwave power, 20 μW (X-band) and 300 μW (S-band); modulation frequency, 100 kHz; modulation amplitude, 1 mT (X-band) and 0.5 mT (S-band).

splitting originated from the coupling of the ^{59}Co nuclear spin (I = 7/2, natural abundance 100%) with the electronic spin cannot be established by the X-band data. We further measured S-band (3.5 GHz) spectra on the sample containing **3**, which clearly demonstrated the existence of ^{59}Co hyperfine coupling (Figure 2 purple). The hyperfine splitting centered at g = 2.13 is consistent with a pattern involving two ^{59}Co nuclei with almost identical A values having a magnitude ~70 MHz (Figure S6). A spectral simulation including two identical ^{59}Co nuclei is the best solution to account for both X-band and S-band data (see Figure 3 for the simulation parameters, and Figures S6 and S7 for more discussions on the spectral simulations). The relatively small g anisotropy ($g_{max} - g_{min}$ = 0.14) and the small A(^{59}Co) tensor suggest that the spin density may not be predominantly localized on a single Co center. Similar observations have been reported for a [Co(III)$_3$Co(IV)O$_4$] species with a complete spin delocalization on the cluster.[51] In addition, several reported μ-superoxo-dicobalt(III) species have also exhibited an broad S = 1/2 EPR signal at cryogenic temperatures similar to the one observed for **3**.[38-39,45,52-54] Interestingly, these μ-superoxo-dicobalt(III) species have much higher thermal stability than **3** that allows them to be characterized even at room temperature, under which their EPR spectra exhibit much better resolved hyperfine structures.[39,55] Although EPR alone is unable to distinguish between bis-μ-oxo dicobalt(III,IV) and μ-superoxo-dicobalt(III) species, combined evidence obtained from X-ray absorption spectroscopy (XAS), Density Functional Theory (DFT) calculations, and oxygen exchange and C–H bond cleavage reactivities supports that **3** is a mixed-valent Co$^{III,IV}_2$(μ-O)$_2$ diamond core species having a spin-delocalized electronic ground state (*vide infra*).

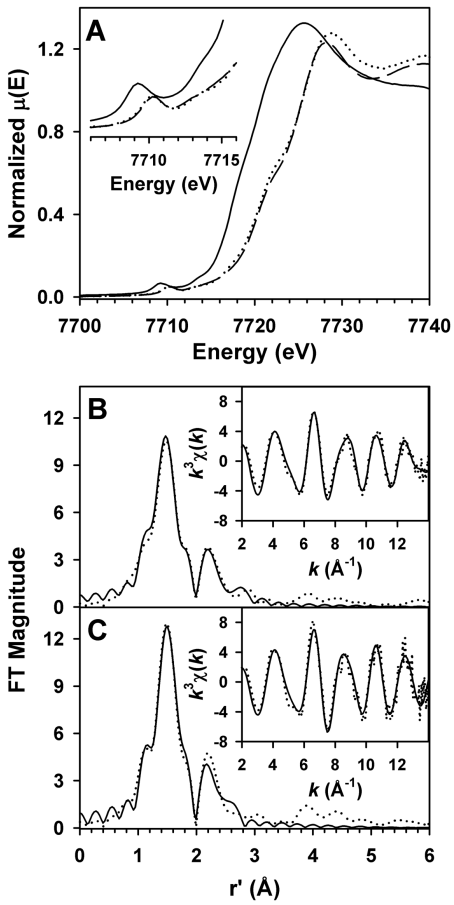

Figure 3. (A) Normalized XANES spectra of **1** (solid line), **2** (dotted line) and **3** (dashed line). The inset depicts an expansion of the pre-edge. (B-C) Representative best fits (bolded entries in Tables S1 and S2) to k^3-weighted EXAFS data of **2** (panel B), and **3** (panel C). Experimental data is shown as a dotted line, while the best fit is shown as a solid line.

Characterization of 2 and 3 by XAS. In light of the thermal instability of both **2** and **3** precluding the growth of suitable single crystals for X-ray crystallography, we turned to cobalt K-edge XAS on frozen solution samples of **2** and **3** for insights into their geometric and electronic structures. To provide further evidence for the progressive oxidation of **1** to **2** and **3**, we first evaluated their cobalt K-edge X-ray absorption near edge spectroscopy (XANES) properties. The XANES spectrum of **2** shows a significant blue shift relative to that of **1,** as evidenced by a +0.9 eV shift of pre-edge energy, and +2.8 eV shift for edge energy (Table 1, Figures 3A and S8), indicating an increase of the Co oxidation state in **2** relative to **1**. Further, after correcting for the yield in the frozen solution samples of **3** (based on quantification of its EPR signal) by normalizing the spectrum after taking a scaled difference of **2** from **3**, the edge energy of **3** is blue-shifted by ~+0.6 eV compared to that of **2** (7720.2 eV for **2** and 7720.8 eV for **3**; see Table 1, Figures 3A and S9) while the pre-edge peak energy (7710.2 eV for both) is invariant (Figure S8). This is consistent with a partial increase of Z_{eff} from **2** to **3**. We note that a small blue shift of the edge energy, without any change in pre-edge peak energy, was similarly observed for Co_4O_4 clusters.[56-57] The pre-edge area of the 7710.2 eV feature is 6.7(2) and 9.0(4) units for **2** and **3**, respectively. There is an additional pre-edge feature at ~7713 eV that gains intensity upon oxidation of **2** (1.7 units) to **3** (5.9 units). The weak in-

tensities of the 1s→3d pre-edge features of complexes **2** and **3** are consistent with O_h symmetry.[58-60] For octahedral low-spin Co(III) centers, the only allowed excited electron configuration is $(t_{2g})^6(e_g)^1$, producing a ^2E_g state.[57-58] This is responsible for the pre-edge feature at 7710 eV for complex **2**. The pre-edge spectrum of mixed-valent complex **3** is expected to be an average of those of its spectroscopically resolved low-spin cobalt(III) and cobalt(IV) centers, as the XAS core-hole lifetime is orders of magnitude shorter than the intramolecular electron transfer rates for class III mixed valent complexes.[57-58,61] For octahedral low-spin Co(IV) centers, the pre-edge peak originates from $^1T_1$, $^3T_1$, and $^1T_2$ excited states of the $(t_{2g})^5(e_g)^1$ electron configuration;[57-58] a transition to the $^1A_1$ excited state from the $(t_{2g})^6(e_g)^0$ electron configuration is expected to produce a lower-energy shoulder, which is not well resolved in the XANES spectrum of complex **3** with mixed-valent Co(III)(μ-O)$_2$Co(IV) core. There is a shoulder on the rising edge at ~7713 eV that gains intensity upon oxidation of **2** (1.7 units) to **3** (5.9 units). Similar features at a relative position of 3~5 eV above the pre-edge peak were observed in $K_3[Fe(III)(CN)_6]$ (octahedral low-spin d^5 system),[61] $K_3[Co(III)(CN)_6]$ (octahedral low-spin d^6 system),[60] several Co(III)-peroxo complexes supported by macrocyclic N_4 ligands (distorted octahedral low-spin d^6 system),[62] and cobalt(III) intermediates of B_{12} enzymes and model compounds supported by dimethylglyoxime ligands with various axial donors (distorted octahedral low-spin d^6 system with or without Co–C bonds);[59] these features were attributed to charge transfer transitions into predominantly ligand-based orbitals and/or 1s-to-4p transitions with shakedown contributions. Such features were also reported for $MCoO_2$ (M = Li, Ag, Eu, and La)[63] and Co_4O_4 cubanes,[57] and were assigned to transitions to orbitals with significant M/M coupling interactions mediated by the oxo bridges.[64] In addition, the $^3T_2$ transition of the excited $(t_{2g})^5(e_g)^1$ electron configuration for the Co(IV) center of complex **3** could also contribute to the broad 7713 eV feature.[57-58]

Extended X-ray absorption fine structure (EXAFS) characterization of **2** and **3** provided further structural insights. The $k^3\chi(k)$ EXAFS of **2** and **3** have highly analogous oscillation patterns, which is mirrored by the very similar appearance of the EXAFS Fourier transforms for these two species (Figures 3B, C). Both observations suggest that the coordination environment around the cobalt centers does not alter appreciably upon the oxidation of **2** to **3**. Indeed, the first coordination shell of **2** and **3** are both best fit by 5 N/O scatterers surrounding the cobalt center at an average distance of 1.91-1.92 Å, accounting for nitrogen donors from the TPA ligand as well as oxo donors. Attempts to split this shell into two subshells of N_{TPA} and O_{oxo} donors yielded poorer quality fits, as evidenced by higher reduced χ^2 and R-factor values. As shown in the DFT geometry-optimized structures (*vide infra*), the N_{TPA} and O_{oxo} subshells are separated by less than the EXAFS resolution of 0.13 Å for our *k* range of 2.0-14.0 Å^{-1}. Therefore, the shorter O_{oxo} sub-shell is not resolved from the N_{TPA} scatterers.

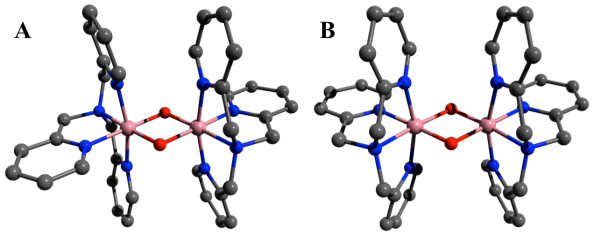

Figure 4. BP86/6-31G(D) optimized symmetric diamond core structures for **3** in the *trans*- (panel A) and *cis*- (panel B) configuration. Cobalt: pink, oxygen: red, nitrogen: blue, carbon: gray, hydrogen atoms are omitted for clarity.

The second coordination sphere for both complexes is best modeled with a combination of long range carbon scatterers and a Co•••Co vector, with the best structural solution for both complexes (i.e. Fit 17 for **2** in Table S1 and Fit 18 for **3** in Table S2) including a cobalt scatterer at a short distance of 2.78 Å away from the absorbing cobalt. Fits excluding this cobalt scatterer and comprising only first-shell N/O scatterers and one or two shells of second sphere C atoms yielded sizably worsened fit quality. The improvement of fit quality by introducing the cobalt scatterer is also observed in the Fourier transform spectrum (Figures S10 and S11). Such a short Co•••Co distance has previously been reported for the crystal structures of $Co^{III}_2(\mu\text{-}O)_2$ complexes (2.67-2.74 Å)[30-35] and other high-valent $M_2(\mu\text{-}O)_2$ complexes with a diamond-core structure (Table S3), and is also confirmed in our DFT geometry optimization (*vide infra*). Notably for both complexes, we did not observe significant features at path-lengths longer than 3 Å in the Fourier transform characteristic of peroxo-bridged core structures such as $Co^{III}(\mu\text{-}OH)(\mu\text{-}OO)Co^{III}$ and $Cu^{II}(\mu\text{-}\eta^2\text{:}\eta^2(O_2))Cu^{II}$ where the M•••M separation is significantly longer (Table S3). Taken together, the characterizations of **2** and **3** by EXAFS support their structural assignment as the $Co_2(\mu\text{-}O)_2$ diamond core complexes.

DFT calculations of 2 and 3. We then turned to DFT opti-

Table 1. Summary of spectroscopic parameters for cobalt species **1**, **2** and **3**.

Complex	λ_{max}, nm (ε, M^{-1} cm^{-1})	Spin State	g_1, g_2, g_3	Pre-edge peak		Rising-edge shoulder		Edge energy (eV)	Co•••Co (Å)
				E (eV)	Area	E (eV)	Area		
1	490 (250) 615 (150)	3/2	7.13, 3.03, 2.06[a]	7709.3(1)	10.7(4)	7713.9(2)	10.1(15)	7717.4	NA
2	460 (4,700)	0	NA	7710.2(1)	6.7(2)	7713.1(1)	1.7(5)	7720.2	2.78[d] 2.784[e]
3	480 (15,000)	1/2	2.14, 2.02, 1.98	7710.2(1)	8.4(3)[b] 9.0(4)[c]	7713.4(1)	4.9(16)[b] 5.9(19)[c]	7720.5[b] 7720.8[c]	2.78[d] 2.769[e]

[a] effect *g* values from m_s = +/- ½ levels of an $\underline{S}$ = 3/2 spin state. [b] from fittings of the raw data. Pre-edge areas are multiplied by100 for convenience. [c] from fittings after correction for the formation yield determined by EPR of the corresponding species. [d] from EXAFS analysis. [e] from geometry optimized calculation.

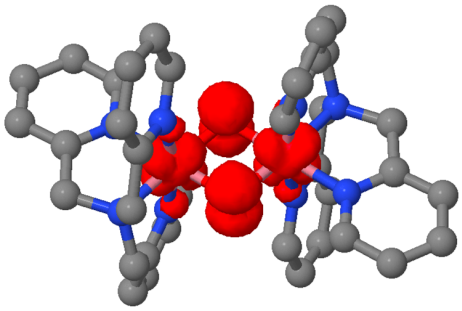

Figure 5. Spin density plot of **3** [BP86/6-31G(D)+PCM(CH_3OH)].

mization of the structures of **2** and **3** (Figures S12 and 4, respectively; also see Table S4) to substantiate our spectroscopic observations. Geometry optimization at the BP86/6-31G(D) level provided low-spin ground states for **2** and **3**, i.e. singlet and doublet, respectively. For each species calculated, an optimized structure with a symmetric $Co_2(\mu\text{-}O)_2$ diamond core and coordinatively saturated cobalt centers was successfully obtained. Two structural isomers differing in the relative position of two tertiary amine nitrogen atoms (i.e. *cis*- vs. *trans*-, see Figures 4, S12 and Scheme S1) were optimized. For both **2** and **3**, the *trans* model was found to be 31.1 kJ/mol and 27.4 kJ/mol lower in energy than the *cis*- model, respectively. In addition to symmetric $Co_2(\mu\text{-}O)_2$ structures, we also optimized open-core and asymmetric $Co_2(\mu\text{-}O)_2$ structures (Scheme S1). However, all of these alternative structures of **2** and **3** are energetically less stable than the symmetric *trans*-$Co_2(\mu\text{-}O)_2$ counterparts. Notably, spin density on the two Co atoms was distributed equally in complex **3** (Figures 5 and S13, Table S5), which implies that **3** is a valence-delocalized system in agreement with the simulation of the EPR data. The Co•••Co distances in the DFT-optimized *trans* structure of **2** and **3** are 2.78 Å and 2.77 Å, respectively, consistent with those determined by EXAFS analysis (Table 1). Furthermore, the average distances of Co–N_{TPA}/O_{oxo} bonds for the *trans* structures of complexes **2** and **3** are 1.92 Å and 1.91 Å (Table S6), respectively, in excellent agreement with EXAFS analysis for the first coordination shell. The average distances of Co–O_{oxo} bonds of DFT geometry optimized *trans* structures **2** and **3** are 1.86 Å and 1.83 Å, respectively. These Co–O_{oxo} distances are consistent with those of several Co_4O_4 cubane complexes with six-coordinated cobalt sites (values are from X-ray crystallography and DFT calculations),[57,65] and are slightly longer than those of diamond core Co_2O_2 crystal structures with cobalt centers of lower coordination numbers (1.78-1.83 Å).[30-35] Furthermore, these geometry-optimized structures clearly showed that the six pyridines are in two distinct local environments with a ratio of 2:1, which is experimentally observed in our ^{1}H NMR results obtained for **2** (*vide supra*, Figure S4). Similar results were obtained using other commonly used DFT functionals M06-L, B3LYP* (15% HF), and B3LYP (Table S7).

C–H bond cleavage reactivity of 3. With the spectroscopic characterization of the mixed-valent $Co^{III,IV}_2(\mu\text{-}O)_2$ diamond core **3** in hand, we sought to investigate its ability to cleave aliphatic C–H bonds. Similar reactivity has yet to be described for superoxo-bridged dicobalt(III) species. We first selected 9,10-dihydroanthracene (DHA, BDE = 78 kcal/mol) as a diagnostic substrate. As shown in Figure S14, the introduction of 8 mM DHA into a freshly prepared solution of **3** at -60 °C in 2:1 methanol/DCM mixed-solvent caused the com-

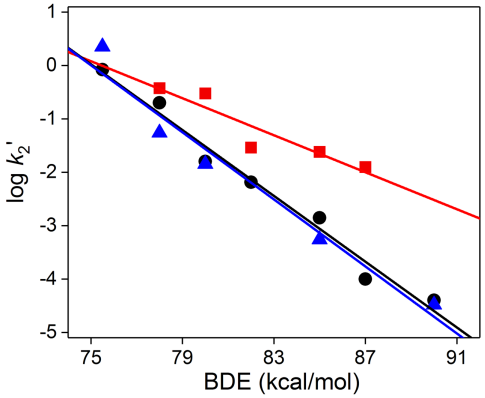

Figure 6. Plot of log k_2' as a function of the C–H bond strength for substrate oxidation by **3** in methanol at -60 °C (red), $Fe^{III,IV}_2(\mu\text{-}O)_2$ with 1 M H_2O at -30 °C (black) and $Cu^{III}_2(\mu\text{-}O)_2$ at -70 °C (blue). The lines represent the best linear fittings.

plete disappearance of its absorption maximum at 480 nm within less than 2 minutes. The kinetic trace could be well fitted using a first-order model to obtain the pseudo-first-order rate constant (k_{obs}) of 0.019 s^{-1}. Furthermore, the second-order rate constant k_2 of 1.5(1) M^{-1} s^{-1} for DHA oxidation could be extracted from the slope of a linear correlation between k_{obs} and the substrate concentration. When deuterated DHA-d_4 was used as the substrate, a slower reaction with k_2 = 0.25(1) M^{-1} s^{-1} was observed, yielding a H/D kinetic isotope effect (KIE) of 6.0 (Figure S15). The large KIE value indicates that the cleavage of an aliphatic C–H bond of DHA by **3** through hydrogen atom transfer (HAT) is the rate-determining step. We further measured the DHA oxidation rate constants in a temperature range of -55 °C to -70 °C, and obtained the activation parameters ($\Delta H^{\neq}$ = 9.0(1) kcal/mol and $\Delta S^{\neq}$ = -14.8(2) cal/(mol•K)) by Eyring analysis (Figure S16). The small activation energy is consistent with the fast rate of DHA oxidation even at cryogenic temperatures.

Quantification of the oxidation product(s) of DHA by GC-MS indicated the formation of primarily anthraquinone (19% yield) and trace amount of anthrone and anthracene, accounting for ~80% of the oxidizing equivalents used (Table S8). We carried out careful control experiments to exclude possible interference from the excess amount of CAN present in the reaction solution. This observation shows that **3** is a two-electron oxidant. Furthermore, the yield of anthraquinone is independent of the amount of O_2 present in the reaction solution, suggesting that anthraquinone is not the product of a radical auto oxidation by O_2. No ligand oxidation product was found, presumably due to geometric constraints of the ligand backbone and the unlikehood of the intermolecular process between two oxidant molecules. After the reaction, a new cobalt species that is distinct from **2** was formed (Figure S12). Given that **3** is a two-electron oxidant, we hypothesized that this new species is a dicobalt(II,III) complex. The characterization of this species will be described elsewhere.

We investigated the reaction of **3** with other hydrocarbons whose C–H bond strength varies in a range of 78-87 kcal/mol. As anticipated, the k_2 value decreases as the C–H bond being cleaved becomes stronger (Figure S17). The benzylic C–H bond of ethylbenzene (BDE = 87 kcal/mol) is the strongest one that **3** can cleave, with a rate of 0.025(2) M^{-1} s^{-1} at -60 °C. Product analysis showed the formation of acetophenone as the

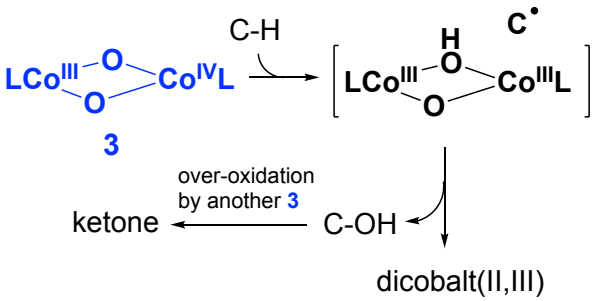

Scheme 2. Proposed mechanism for C–H bond oxygenation by complex **3**.

only product at the yield of 15%, accounting for ~43% (after correcting for the formation yield of **3**) of the oxidizing equivalents available for **3**. The oxidizing equivalents unaccounted for may be due to the self-decay of **3**, which has first-order rate constant of ~0.008 s^{-1}. Furthermore, a H/D KIE of 8.8 and 7.8 was determined for the oxidation of fluorene and ethylbenzene (Figures S18 and S19), respectively, clearly indicating that **3** cleaves the C–H bond of these substrates *via* a HAT process. For this group of substrates studied, the logarithm of k_2' (k_2' = k_2/number of equivalent hydrogen), when normalized on a per hydrogen basis, correlated linearly with the strength of the C–H bond being cleaved with a slope of -0.17 (Figure 6). The analysis of product formation for these substrates showed that ketone was the primary product (Table S7). In some cases alcohol and desaturated products were also formed but in much smaller yields.

3 is thus an oxygenation reagent for C–H bonds. The rate-determining HAT process from the substrate likely generates a $Co^{III}_2(\mu\text{-O})(\mu\text{-OH})$ species and a carbon centered radical. The rebound of the hydroxyl group back to the carbon radical then yields the hydroxylated C–OH product (Scheme 2). The over-oxidation of the alcohol product must occur by another molecule of **3** to generate the ketone product observed in product analysis. Our observation that the product distribution and yield are independent of the presence of O_2 in the reaction media indicates that the rebound of the hydroxyl group to the carbon radical must be fast so that the carbon radical does not escape from the radical cage to be trapped by O_2.

We further studied the exchange kinetics of the oxo ligands in complexes **2** and **3** with added $H_2{}^{18}O$ in methanol at -60 °C in order to understand this fundamental reactivity of bis-μ-oxo complexes.[66-67] In these experiments, $H_2{}^{18}O$ was either added to the solution of **2**, allowing oxygen exchange to occur for a period of incubation time followed by rapid conversion of **2** to **3**, or introduced directly to the solution of **3** for oxygen exchange. The addition of water does not affect the formation yield of **3**. We then employed ethylbenzene as a substrate probe to react with **3**, and monitored the incorporation of ^{18}O isotope in the oxidation product acetophenone by GC-MS. Complex **2** has sufficient lifetime at -60 °C that allows us to vary the incubation time up to 4 hours after the addition of $H_2{}^{18}O$. In contrast, complex **3** is too short-lived for a similar set of incubation time dependence studies.

As shown in Figure 7A, the incorporation of ^{18}O isotope in acetophenone was found to be 17% when 0.3 M $H_2{}^{18}O$ was added to the solution of **2** without any incubation time. The fraction of ^{18}O acetophenone increases when increasing the incubation time of the solution of **2** after the same amount of $H_2{}^{18}O$ was added (Figure 7A), up to 35% at the maximum

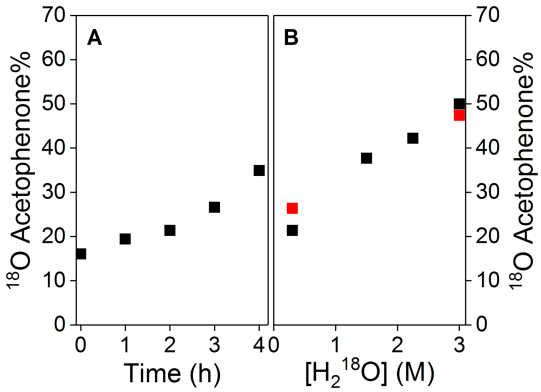

Figure 7. Plots of the ^{18}O incorporation percentage in acetophenone as a function of (A) incubation time after 0.3 M $H_2{}^{18}O$ was added to 3 mM **2**, and (B) the concentration of $H_2{}^{18}O$ introduced to either 3 mM **2** with a 2-hour incubation time (black squares) or 3 mM **3** with no incubation time (red squares). Other conditions: in methanol at -60 °C.

tested incubation time of 4 hours. This slight dependence of the ^{18}O incorporation as a function of the incubation time indicates that oxygen exchange on complex **2** is in fact slow (within hours), consistent with the kinetic inertness of low-spin Co(III) centers.[68] Furthermore, the fraction of ^{18}O acetophenone increases as a function of the concentration of $H_2{}^{18}O$ added to the solution of **2** with a fixed incubation time (2 hours, Figure 7B). At the maximum $H_2{}^{18}O$ concentration tested (3 M, almost the saturation concentration in methanol at -60 °C), we observed ~50% ^{18}O incorporation in acetophenone. In addition, we performed a set of control experiments by adding $H_2{}^{18}O$ directly to the solution of **3** followed by immediate ethylbenzene oxidation (without any incubation time). For the two $H_2{}^{18}O$ concentrations tested (red data points in Figure 7B), comparable ^{18}O acetophenone contents were obtained compared to the set of studies in which $H_2{}^{18}O$ was added to complex **2** with a 2-hour incubation time (black data points in Figure 7B). This observation suggests that oxygen exchange proceeds much faster on **3** than on **2.**

These data thus provide strong support for the structural assignment of **2** and **3** as having the bis-μ-oxo diamond cores, since the oxygen exchange of $H_2{}^{18}O$ with peroxo- and superoxo-bridged dinuclear species is highly unlikely. Furthermore, the incorporation of ^{18}O isotope into the reaction product of ethylbenzene is a clear demonstration that the oxygen in acetophenone is from the diamond core complex **3**. This observation is consistent with the rebound mechanism (Scheme 2) proposed for C–H bond oxygenation reactions.

Our results clearly revealed that the $Co^{III,IV}_2(\mu\text{-O})_2$ diamond core **3** is a highly reactive oxidant towards C–H bonds. The BDE plots shown in Figure 6 comparing C–H bond cleavage reactivities of **3** with $Fe^{III,IV}_2(\mu\text{-O})_2$ (in the presence of 1 M H_2O)[22] and $Cu^{III}_2(\mu\text{-O})_2$ (in an equilibrium with a $Cu^{II}_2(\mu\text{-}\eta:\eta\text{-}O_2)$ species)[23] showed that **3** is up to two orders of magnitude more reactive than the other two diamond core species. The slope of the linear fitting for **3** (-0.17) is less steep than those of $Fe^{III,IV}_2(\mu\text{-O})_2$ and $Cu^{III}_2(\mu\text{-O})_2$ species (~-0.3), indicating that the rate constants of **3** are less sensitive to the C–H bond strength of the substrates than the other two species.

Specifically, **3** has the highest reaction rate for DHA oxidation (1.5 M^{-1} s^{-1} at -60 °C) compared to diamond core com-

plexes of other first-row transition metals including Mn,[17] Fe[69] and Cu[23] reported previously at a variety of temperatures (see also Table S9 and references therein). **3** is about 3 orders of magnitude more reactive than the di-manganese species $Mn^{III,IV}_2(\mu\text{-}O)_2$ (1.2×10^{-3} M^{-1} s^{-1} at 32 °C),[17] and is about 4-5 orders of magnitude more reactive than the diiron analogs $Fe^{III,IV}_2(\mu\text{-}O)_2$ and $Fe^{IV}_2(\mu\text{-}O)_2$ supported by TPA and related ligands (10^{-4}-10^{-5} M^{-1} s^{-1} at -30 °C).[69] Furthermore, **3** oxidizes ethylbenzene at a rate of 0.025(2) M^{-1} s^{-1} at -60 °C, which is about two orders of magnitude faster than that of $Fe^{III,IV}_2(\mu\text{-}O)_2$ at -30 °C in the presence of 1 M H_2O (2×10^{-4} M^{-1} s^{-1}).[22] Surprisingly, the redox potential of **3** (0.27-0.49 V) is comparable or even lower than those of these two high-valent diiron counterparts.[69] Therefore, other factors such as the pK_a of the bridging oxo ligands and the activation energy of cleaving a C–H bond likely contribute to the high reactivity of **3**. On the other hand, **3** is unable to cleave C–H bonds stronger than 87 kcal/mol. This thermodynamic limit likely reflects the strength of the $Co^{III}O$–H bond formed after the HAT step. Our ongoing investigations aim to measure these thermodynamic values in order to better understand the reactivity of **3**.

In addition, the DHA oxidation rate of **3** is at least 7-fold higher than those measured at higher temperatures of two mononuclear oxocobalt(IV) species recently described.[25-26] In fact, the DHA oxidation rate is only about one order of magnitude slower than the one measured for the open core species $HO\text{-}Fe^{III}\text{-}O\text{-}Fe^{IV}{=}O$ (28 M^{-1} s^{-1}).[70] It is thus conceivable that further development of this high-valent dicobalt-oxo system could lead to the generation of even more reactive species for sp^3 C–H bond activation.

Conclusion.

In conclusion, we have generated an unprecedented high-valent dicobalt(III,IV) complex $Co^{III,IV}_2(\mu\text{-}O)_2$ **3** by one-electron oxidation of its $Co^{III}_2(\mu\text{-}O)_2$ precursor **2**. Characterization of **3** by spectroscopic and computational methods including EPR, XAS and DFT revealed that **3** has an S =1/2 ground state and a bis-μ-oxo diamond core structure (preferably in a *trans* configuration) with a short Co•••Co distance. The bridging oxo ligands of **3** are exchangeable with $H_2{}^{18}O$. **3** is able to cleave C–H bonds having bond strength up to 87 kcal/mol, affording fast kinetic rate constants and the oxygenated products. These features (spectroscopy, stability and reactivity) are distinct from those of the peroxo- and superoxo-bridged dicobalt(III) complexes supported by the same TPA ligand recently reported by other groups.[38-39] Interestingly, the rate constant for DHA oxidation by **3** is 4-5 orders of magnitude higher than those determined for the diiron analogs, despite the fact that **3** has a moderate redox potential that is comparable to those of the diiron species. These interesting findings shed light on better understanding of the high-valent diamond core chemistry for cobalt and inspire future development of more effective approaches for C–H bond activation by bio-inspired dicobalt complexes.

ASSOCIATED CONTENT

Supporting Information

Experimental methods, computational details, Figures S1-S19, Table S1-S22, Scheme S1.

The Supporting Information is available free of charge on the ACS Publications website.

AUTHOR INFORMATION

Corresponding Author

*E-mail: dong1.wang@umontana.edu; talipovm@nmsu.edu; fli@nmsu.edu

ORCID

Yisong Guo: 0000-0002-4132-3565
Marat Talipov: 0000-0002-7559-9666
Feifei Li: 0000-0001-6657-2042
Dong Wang: 0000-0002-6370-1942

Notes

The authors declare no competing financial interest.

ACKNOWLEDGMENT

Support of this work was provided by the Center for Biomolecular Structure and Dynamics CoBRE (Grant NIGMS P20GM103546) and the University of Montana (Y.L. and D.W.). F.L., M.R.T. and S.H. are supported by New Mexico State University start-up funding. Y.G. acknowledges the support from NSF (CHE-1654060). We thank Mr. Ruixi Fan at CMU for assisting with EPR measurements. E.R.F. was supported by NIH P30-EB-009998. Use of beamline 7-3 at the Stanford Synchrotron Radiation Lightsource (SLAC National Accelerator Laboratory) was made possible by the US Department of Energy, Office of Basic Energy Sciences under Contract No. DE-AC02-76SF00515 and support of the SSRL Structural Molecular Biology Program by the DOE Office of Biological and Environmental Research as well as the NIH. The computational studies were supported by the Extreme Science and Engineering Discovery Environment (XSEDE), project number TG-CHE170004.

REFERENCES

(1) Yang, X.; Wu, T.; Phipps, R. J.; Toste, F. D. Advances in Catalytic Enantioselective Fluorination, Mono-, Di-, and Trifluoromethylation, and Trifluoromethylthiolation Reactions. *Chem. Rev.* **2015**, *115*, 826-870.

(2) Furuya, T.; Kamlet, A. S.; Ritter, T. Catalysis for Fluorination and Trifluoromethylation. *Nature* **2011**, *473*, 470-477.

(3) Purser, S.; Moore, P. R.; Swallow, S.; Gouverneur, V. Fluorine in Medicinal Chemistry. *Chem. Soc. Rev.* **2008**, *37*, 320-330.

(4) Miller, P. W.; Long, N. J.; Vilar, R.; Gee, A. D. Synthesis of ^{11}C, ^{18}F, ^{15}O, and ^{13}N Radiolabels for Positron Emission Tomography. *Angew. Chem. Int. Ed.* **2008**, *47*, 8998-9033.

(5) Ametamey, S. M.; Honer, M.; Schubiger, P. A. Molecular Imaging with PET. *Chem. Rev.* **2008**, *108*, 1501-1516.

(6) Brase, S.; Gil, C.; Knepper, K.; Zimmermann, V. Organic Azides: An Exploding Diversity of a Unique Class of Compounds. *Angew. Chem. Int. Ed.* **2005**, *44*, 5188-5240.

(7) Thirumurugan, P.; Matosiuk, D.; Jozwiak, K. Click Chemistry for Drug Development and Diverse Chemical-Biology Applications. *Chem. Rev.* **2013**, *113*, 4905-4979.

(8) Huang, X.; Groves, J. T. Beyond Ferryl-mediated Hydroxylation: 40 Years of the Rebound Mechanism and C–H Activation. *J. Biol. Inorg. Chem.* **2017**, *22*, 185-207.

(9) Jasniewski, A. J.; Que, L., Jr. Dioxygen Activation by Nonheme Diiron Enzymes: Diverse Dioxygen Adducts, High-Valent Intermediates, and Related Model Complexes. *Chem. Rev.* **2018**, *118*, 2554-2592.

(10) Wallar, B. J.; Lipscomb, J. D. Dioxygen Activation by Enzymes Containing Binuclear Non-Heme Iron Clusters. *Chem. Rev.* **1996**, *96*, 2625-2657.

(11) Shu, L.; Nesheim, J. C.; Kauffmann, K.; Münck, E.; Lipscomb, J. D.; Que, L., Jr. An $Fe^{IV}_2O_2$ Diamond Core Structure for the Key Intermediate Q of Methane Monooxygenase. *Science* **1997**, *275*, 515-518.

(12) Liu, K. E.; Wang, D.; Huynh, B. H.; Edmondson, D. E.; Salifoglou, A.; Lippard, S. J. Spectroscopic Detection of Intermediates in the Reaction of Dioxygen with the Reduced Methane Monooxygenase Hydroxylase from Methylococcus capsulatus (Bath). *J. Am. Chem. Soc.* **1994**, *116*, 7465-7466.

(13) Lee, S.-K.; Fox, B. G.; Froland, W. A.; Lipscomb, J. D.; Münck, E. A Transient Intermediate of the Methane Monooxygenase Catalytic Cycle Containing an $Fe^{IV}Fe^{IV}$ Cluster. *J. Am. Chem. Soc.* **1993**, *115*, 6450-6451.

(14) Banerjee, R.; Proshlyakov, Y.; Lipscomb, J. D.; Proshlyakov, D. A. Structure of the Key Species in the Enzymatic Oxidation of Methane to Methanol. *Nature* **2015**, *518*, 431-435.

(15) Castillo, R. G.; Banerjee, R.; Allpress, C. J.; Rohde, G. T.; Bill, E.; Que, L., Jr.; Lipscomb, J. D.; DeBeer, S. High-Energy-Resolution Fluorescence-Detected X-ray Absorption of the Q Intermediate of Soluble Methane Monooxygenase. *J. Am. Chem. Soc.* **2017**, *139*, 18024-18033.

(16) Cutsail, G. E., III.; Banerjee, R.; Zhou, A.; Que, L., Jr.; Lipscomb, J. D.; DeBeer, S. High-Resolution Extended X-ray Absorption Fine Structure Analysis Provides Evidence for a Longer Fe···Fe Distance in the Q Intermediate of Methane Monooxygenase. *J. Am. Chem. Soc.* **2018**, *140*, 16807-16820.

(17) Larsen, A. S.; Wang, K.; Lockwood, M. A.; Rice, G. L.; Won, T.-J.; Lovell, S.; Sadılek, M.; Turecek, F.; Mayer, J. M. Hydrocarbon Oxidation by Bis-μ-oxo Manganese Dimers: Electron Transfer, Hydride Transfer, and Hydrogen Atom Transfer Mechanisms. *J. Am. Chem. Soc.* **2002**, *124*, 10112-10123.

(18) Wang, K.; Mayer, J. M. Oxidation of Hydrocarbons by $[(phen)_2Mn(\mu\text{-}O)_2Mn(phen)_2]^{3+}$ via Hydrogen Atom Abstraction. *J. Am. Chem. Soc.* **1997**, *119*, 1470-1471.

(19) Das, S.; Incarvito, C. D.; Crabtree, R. H.; Brudvig, G. W. Molecular Recognition in the Selective Oxygenation of Saturated C–H Bonds by a Dimanganese Catalyst. *Science* **2006**, *312*, 1941-1943.

(20) Young, K. J.; Brennan, B. J.; Tagore, R.; Brudvig, G. W. Photosynthetic Water Oxidation: Insights from Manganese Model Chemistry. *Acc. Chem. Res.* **2015**, *48*, 567-574.

(21) Wang, D.; Farquhar, E. R.; Stubna, A.; Münck, E.; Que, L., Jr. A Diiron(IV) Complex that Cleaves Strong C–H and O–H Bonds. *Nat. Chem.* **2009**, *1*, 145-150.

(22) Xue, G.; Pokutsa, A.; Que, L., Jr. Substrate-Triggered Activation of a Synthetic $[Fe_2(\mu\text{-}O)_2]$ Diamond Core for C–H Bond Cleavage. *J. Am. Chem. Soc.* **2011**, *133*, 16657-16667.

(23) Matsumoto, T.; Ohkubo, K.; Honda, K.; Yazawa, A.; Furutachi, H.; Fujinami, S.; Fukuzumi, S.; Suzuki, M. Aliphatic C–H Bond Activation Initiated by a $(\mu\text{-}\eta^2\text{:}\eta^2\text{-Peroxo})$dicopper(II) Complex in Comparison with Cumylperoxyl Radical. *J. Am. Chem. Soc.* **2009**, *131*, 9258-9267.

(24) Elwell, C. E.; Gagnon, N. L.; Neisen, B. D.; Dhar, D.; Spaeth, A. D.; Yee, G. M.; Tolman, W. B. Copper-Oxygen Complexes Revisited: Structures, Spectroscopy, and Reactivity. *Chem. Rev.* **2017**, *117*, 2059-2107.

(25) Wang, B.; Lee, Y.-M.; Tcho, W.-Y.; Tussupbayev, S.; Kim, S.-T.; Kim, Y.; Seo, M. S.; Cho, K.-B.; Dede, Y.; Keegan, B. C.; Ogura, T.; Kim, S. H.; Ohta, T.; Baik, M.-H.; Ray, K.; Shearer, J.; Nam, W. Synthesis and Reactivity of a Mononuclear Non-haem Cobalt(IV)-oxo Complex. *Nat. Commun.* **2017**, *8*, 14839.

(26) Hong, S.; Pfaff, F. F.; Kwon, E.; Wang, Y.; Seo, M.-S.; Bill, E.; Ray, K.; Nam, W. Spectroscopic Capture and Reactivity of a Low-Spin Cobalt(IV)-Oxo Complex Stabilized by Binding Redox-Inactive Metal Ions. *Angew. Chem. Int. Ed.* **2014**, *53*, 10403-10407.

(27) Surendranath, Y.; Kanan, M. W.; Nocera, D. G. Mechanistic Studies of the Oxygen Evolution Reaction by a Cobalt-phosphate Catalyst at Neutral pH. *J. Am. Chem. Soc.* **2010**, *132*, 16501-16509.

(28) Nguyen, A. I.; Ziegler, M. S.; Oña-Burgos, P.; Sturzbecher-Hohne, M.; Kim, W.; Bellone, D. E.; Tilley, T. D. Mechanistic Investigations of Water Oxidation by a Molecular Cobalt Oxide Analogue: Evidence for a Highly Oxidized Intermediate and Exclusive Terminal Oxo Participation. *J. Am. Chem. Soc.* **2015**, *137*, 12865-12872.

(29) Ray, K.; Heims, F.; Pfaff, F. F. Terminal Oxo and Imido Transition-Metal Complexes of Groups 9-11. *Eur. J. Inorg. Chem.* **2013**, 3784-3807.

(30) Hikichi, S.; Yoshizawa, M.; Sasakura, Y.; Komatsuzaki, H.; Moro-oka, Y.; Akita, M. Structural Characterization and Intramolecular Aliphatic C-H Oxidation Ability of $M^{III}(\mu\text{-}O)_2M^{III}$ Complexes of Ni and Co with the Hydrotris-(3,5-dialkyl-4-X-pyrazolyl)borate Ligands $Tp^{Me2,X}$ (X = Me, H, Br) and Tp^{iPr2}. *Chem. Eur. J.* **2001**, *7*, 5011-5028.

(31) Larsen, P. L.; Parolin, T. J.; Powell, D. R.; Hendrich, M. P.; Borovik, A. S. Hydrogen Bonds around $M(\mu\text{-}O)_2M$ Rhombs: Stabilizing a $\{Co^{III}(\mu\text{-}O)_2Co^{III}\}$ Complex at Room Temperature. *Angew. Chem. Int. Ed.* **2003**, *42*, 85-89.

(32) Dai, X.; Kapoor, P.; Warren, T. H. $[Me_2NN]Co(\eta^6\text{-toluene})$: O=O, N=N, and O=N Bond Cleavage Provides β-Diketiminato Cobalt μ-Oxo and Imido Complexes. *J. Am. Chem. Soc.* **2004**, *126*, 4798-4799.

(33) Zhao, P.; Lei, H.; Ni, C.; Guo, J.-D.; Kamali, S.; Fettinger, J. C.; Grandjean, F.; Long, G. J.; Nagase, S.; Power, P. P. Quasi-Three-Coordinate Iron and Cobalt Terphenoxide Complexes $\{Ar^{iPr8}OM(\mu\text{-}O)\}_2$ (Ar^{iPr8} = C_6H-2,6-(C_6H_2-2,4,6-$^iPr_3$)$_2$-3,5-$^iPr_2$; M = Fe or Co) with $M(III)_2(\mu\text{-}O)_2$ Core Structures and the Peroxide Dimer of 2-Oxepinoxy Relevant to Benzene Oxidation. *Inorg. Chem.* **2015**, *54*, 8914-8922.

(34) DeRosha, D. E.; Mercado, B. Q.; Lukat-Rodgers, G.; Rodgers, K. R.; Holland, P. L. Enhancement of C–H Oxidizing Ability in Co–O_2 Complexes through an Isolated Heterobimetallic Oxo Intermediate. *Angew. Chem. Int. Ed.* **2017**, *56*, 3211-3215.

(35) Engelmann, X.; Yao, S.; Farquhar, E. R.; Szilvμsi, T.; Kuhlmann, U.; Hildebrandt, P.; Driess, M.; Ray, K. A New Domain of Reactivity for High-Valent Dinuclear $[M(\mu\text{-}O)_2M']$ Complexes in Oxidation Reactions. *Angew. Chem. Int. Ed.* **2017**, *56*, 297-301.

(36) Hikichi, S.; Yoshizawa, M.; Sasakura, Y.; Akita, M.; Morooka, Y. First Synthesis and Structural Characterization of Dinuclear M(III) Bis(μ-oxo) Complexes of Nickel and Cobalt with Hydrotris(pyrazolyl)borate Ligand. *J. Am. Chem. Soc.* **1998**, *120*, 10567-10568.

(37) Chan, S. L.-F.; Lam, T. L.; Yang, C.; Lai, J.; Cao, B.; Zhou, Z.; Zhu, Q. Cobalt(II) Tris(2-pyridylmethyl)amine Complexes $[Co(TPA)X]^+$ Bearing Coordinating Anion (X = Cl , Br , I and NCS): Synthesis and Application for Carbon Dioxide Reduction. *Polyhedron* **2017**, *125*, 156-163.

(38) Wang, H.-Y.; Mijangos, E.; Ott, S.; Thapper, A. Water Oxidation Catalyzed by a Dinuclear Cobalt–Polypyridine Complex. *Angew. Chem. Int. Ed.* **2014**, *53*, 14499-14502.

(39) Kotani, H.; Hong, D.; Satonaka, K.; Ishizuka, T.; Kojima, T. Mechanistic Insight into Dioxygen Evolution from Diastereomeric m-Peroxo Dinuclear Co(III) Complexes Based on Stoichiometric Electron-Transfer Oxidation. *Inorg. Chem.* **2019**, *58*, 3676-3682.

(40) Ishizuka, T.; Watanabe, A.; Kotani, H.; Hong, D.; Satonaka, K.; Wada, T.; Shiota, Y.; Yoshizawa, K.; Ohara, K.; Yamaguchi, K.; Kato, S.; Fukuzumi, S.; Kojima, T. Homogeneous Photocatalytic Water Oxidation with a Dinuclear CoIII−Pyridylmethylamine Complex. *Inorg. Chem.* **2016**, *55*, 1154-1164.

(41) Meloon, D. R.; Harris, G. M. Preparation, Structure, and Interconversion Kinetics of Mono- and Binuclear Aquo(nitrilotriacetato)cobaltate(III) Complexes. *Inorg. Chem.* **1977**, *16*, 434-437.

(42) Cho, J.; Sarangi, R.; Kang, H. Y.; Lee, J. Y.; Kubo, M.; Ogura, T.; Solomon, E. I.; Nam, W. Synthesis, Structural, and Spectroscopic Characterization and Reactivities of Mononuclear Cobalt(III)-Peroxo Complexes. *J. Am. Chem. Soc.* **2010**, *132*, 16977-16986.

(43) Hu, X.; Castro-Rodriguez, I.; Meyer, K. Dioxygen Activation by a Low-Valent Cobalt Complex Employing a Flexible Tripodal N-Heterocyclic Carbene Ligand. *J. Am. Chem. Soc.* **2004**, *126*, 13464-13473.

(44) Rahman, A. F. M. M.; Jackson, W. G.; Willis, A. C. The First Sideways-Bonded Peroxo Complex for a Tetraaminecobalt(III) Species. *Inorg. Chem.* **2004**, *43*, 7558-7560.

(45) Rigsby, M. L.; Mandal, S.; Nam, W.; Spencer, L. C.; Llobet, A.; Stahl, S. S. Cobalt Analogs of Ru-based Water Oxidation Catalysts: Overcoming Thermodynamic Instability and Kinetic Lability to Achieve Electrocatalytic O_2 Evolution. *Chem. Sci.* **2012**, *3*, 3058-3062.

(46) Shiren, K.; Ogo, S.; Fujinami, S.; Hayashi, H.; Suzuki, M.; Uehara, A.; Watanabe, Y.; Moro-oka, Y. Synthesis, Structures, and Properties of Bis(μ-oxo)nickel(III) and Bis(μ-superoxo)nickel(II) Complexes: An Unusual Conversion of a $Ni^{III}_2(\mu\text{-}O)_2$ Core into a $Ni^{II}_2(\mu\text{-}OO)_2$ Core by H_2O_2 and Oxygenation of Ligand. *J. Am. Chem. Soc.* **2000**, *122*, 254-262.

(47) Itoh, S.; Bandoh, H.; Nakagawa, M.; Nagatomo, S.; Kitagawa, T.; Karlin, K. D.; Fukuzumi, S. Formation, Characterization, and Reactivity of Bis(μ-oxo)dinickel(III) Complexes Supported by A Series of Bis[2-(2-pyridyl)ethyl]amine Ligands. *J. Am. Chem. Soc.* **2001**, *123*, 11168-11178.

(48) McAlpin, J. G.; Surendranath, Y.; Dinca, M.; Stich, T. A.; Stoian, S. A.; Casey, W. H.; Nocera, D. G.; Britt, R. D. EPR Evidence for Co(IV) Species Produced During Water Oxidation at Neutral pH. *J. Am. Chem. Soc.* **2010**, *132*, 6882-6883.

(49) Wang, D.; Groves, J. T. Efficient Water Oxidation Catalyzed by Homogeneous Cationic Cobalt Porphyrins: Critical Roles for the Buffer Base. *Proc. Natl. Acad. Sci. USA* **2013**, *110*, 15579-15584.

(50) Connelly, N. G.; Geiger, W. E. Chemical Redox Agents for Organometallic Chemistry. *Chem. Rev.* **1996**, *96*, 877-910.

(51) McAlpin, J. G.; Stich, T. A.; Ohlin, C. A.; Surendranath, Y.; Nocera, D. G.; Casey, W. H.; Britt, R. D. Electronic Structure Description of a $[Co(III)_3Co(IV)O_4]$ Cluster: A Model for the Paramagnetic Intermediate in Cobalt-Catalyzed Water Oxidation. *J. Am. Chem. Soc.* **2011**, *133*, 15444-15452.

(52) Cho, Y. I.; Joseph, D. M.; Rose, M. J. "Criss-Crossed" Dinucleating Behavior of an N4 Schiff Base Ligand: Formation of a μ-OH, $\mu\text{-}O_2$ Dicobalt(III) Core via O_2 Activation. *Inorg. Chem.* **2013**, *52*, 13298-13300.

(53) Stich, T. A.; McAlpin, J. G.; Wall, R. M.; Rigsby, M. L.; Britt, R. D. Electron Paramagnetic Resonance Characterization of Dioxygen-Bridged Cobalt Dimers with Relevance to Water Oxidation. *Inorg. Chem.* **2016**, *55*, 12728-12736.

(54) Sykes, A. G., et al. In *Progress in Inorganic Chemistry*; Edwards, J. O., Ed.; Wiley: 1970.

(55) Schrauzer, G. N.; Lee, L. P. Cobaloximes(II) and Vitamin B12r as Oxygen Carriers. Evidence for Monomeric and Dimeric Peroxides and Superoxides. *J. Am. Chem. Soc.* **1970**, *92*, 1551-1557.

(56) Brodsky, C. N.; Hadt, R. G.; Hayes, D.; Reinhart, B. J.; Li, N.; Chen, L. X.; Nocera, D. G. In situ Characterization of Cofacial Co(IV) Centers in Co_4O_4 Cubane: Modeling the High-valent Active Site in Oxygen-evolving Catalysts. *Proc. Natl. Acad. Sci. USA* **2017**, *114*, 3855-3860.

(57) Hadt, R. G.; Hayes, D.; Brodsky, C. N.; Ullman, A. M.; Casa, D. M.; Upton, M. H.; Nocera, D. G.; Chen, L. X. X-ray Spectroscopic Characterization of Co(IV) and Metal−Metal Interactions in Co_4O_4: Electronic Structure Contributions to the Formation of High-Valent States Relevant to the Oxygen Evolution Reaction. *J. Am. Chem. Soc.* **2016**, *138*, 11017-11030.

(58) Westre, T. E.; Kennepohl, P.; DeWitt, J. G.; Hedman, B.; Hodgson, K. O.; Solomon, E. I. A Multiplet Analysis of Fe K-Edge 1s -> 3d Pre-Edge Features of Iron Complexes. *J. Am. Chem. Soc.* **1997**, *119*, 6297-6314.

(59) Chance, M. R. In *Chemistry and Biochemistry of B12*; Banerjee, R., Ed.; A Wiley-Interscience Publication: 1999.

(60) Sano, M. XANES Study at the Co K Absorption Edge in a Series of Cobalt(III) Complexes. *Inorg. Chem.* **1988**, *27*, 4249-4253.

(61) DeBeer George, S.; Petrenko, T.; Neese, F. Prediction of Iron K-Edge Absorption Spectra Using Time-Dependent Density Functional Theory. *J. Phys. Chem. A* **2008**, *112*, 12936-12943.

(62) Sarangi, R.; Cho, J.; Nam, W.; Solomon, E. I. XAS and DFT Investigation of Mononuclear Cobalt(III) Peroxo Complexes: Electronic Control of the Geometric Structure in CoO_2 versus NiO_2 Systems. *Inorg. Chem.* **2011**, *50*, 614-620.

(63) de Groot, F. M. F.; Vankó, G.; Glatzel, P. The 1s X-ray Absorption Pre-edge Structures in Transition Metal Oxides. *J. Phys. Condens. Matter* **2009**, *21*, 104207.

(64) Vankó, G.; de Groot, F. M. F.; Huotari, S.; Cava, R. J.; Lorenz, T.; Reuther, M. Intersite 4p-3d Hybridization in Cobalt Oxides: A Resonant x-Ray Emission Spectroscopy Study. *ArXiv.org e-Print Arch., Condens. Matter* **2008**, arXiv:082.2744v2741.[cond-mat.str-el].

(65) Chakrabarty, R.; Bora, S. J.; Das, B. K. Synthesis, Structure, Spectral and Electrochemical Properties, and Catalytic Use of Cobalt(III)-Oxo Cubane Clusters. *Inorg. Chem.* **2007**, *46*, 9450-9462.

(66) Tagore, R.; Crabtree, R. H.; Brudvig, G. W. Distinct Mechanisms of Bridging-Oxo Exchange in Di-μ-O Dimanganese Complexes with and without Water-Binding Sites: Implications for Water Binding in the O_2-Evolving Complex of Photosystem II. *Inorg. Chem.* **2007**, *46*, 2193-2203.

(67) Tagore, R.; Chen, H.; Crabtree, R. H.; Brudvig, G. W. Determination of μ-Oxo Exchange Rates in Di-μ-Oxo Dimanganese Complexes by Electrospray Ionization Mass Spectrometry. *J. Am. Chem. Soc.* **2006**, *128*, 9457-9465.

(68) Lippard, S. J.; Berg, J. M. In *Principles of Bioinorganic Chemistry*; University Science Books: Mill Valley, California, 1994.

(69) Xue, G.; Wang, D.; De Hont, R.; Fiedler, A. T.; Shan, X.; Münck, E.; Que, L., Jr. A Synthetic Precedent for the $[Fe^{IV}_2(\mu\text{-}O)_2]$ Diamond Core Proposed for Methane Monooxygenase Intermediate **Q**. *Proc. Natl. Acad. Sci. USA* **2007**, *104*, 20713-20718.

(70) Xue, G.; Hont, R. D.; Münck, E.; Que, L., Jr. Million-fold Activation of the $[Fe_2(\mu\text{-}O)_2]$ Diamond Core for C–H Bond Cleavage. *Nat. Chem.* **2010**, *2*, 400-405.